








# Surface cleaning and sample carrier for complementary high-resolution imaging techniques

Cite as: Biointerphases **15**, 021005 (2020); <https://doi.org/10.1116/1.5143203>

Submitted: 20 December 2019 . Accepted: 09 March 2020 . Published Online: 25 March 2020

Pietro Benettoni, Jia-Yu Ye, Timothy R. Holbrook, Federica Calabrese,  Stephan Wagner, Mashaalah Zarejousheghani, Jan Griebel, Maria K. Ullrich,  Niculina Musat,  Matthias Schmidt,  Roman Flyunt,  Thorsten Reemtsma,  Hans-Hermann Richnow,  Hryhoriy Stryhanyuk, et al.

## COLLECTIONS

Paper published as part of the special topic on [Special Topic Collection on Secondary Ion Mass Spectrometry \(SIMS\)](#)



View Online



Export Citation



CrossMark

## ARTICLES YOU MAY BE INTERESTED IN

[Ar-gas cluster ion beam in ToF-SIMS for peptide and protein analysis](#)

Biointerphases **15**, 021011 (2020); <https://doi.org/10.1116/6.0000105>

[Numerical evaluation of polyethylene glycol ligand conjugation to gold nanoparticle surface using ToF-SIMS and statistical analysis](#)

Biointerphases **15**, 031008 (2020); <https://doi.org/10.1116/6.0000106>

[TOF-SIMS imaging reveals tumor heterogeneity and inflammatory response markers in the microenvironment of basal cell carcinoma](#)

Biointerphases **15**, 041012 (2020); <https://doi.org/10.1116/6.0000340>






## AVS Quantum Science

### Now Publishing Original Research

Co-Published by




[LEARN MORE](#)








# Surface cleaning and sample carrier for complementary high-resolution imaging techniques

Cite as: *Biointerphases* 15, 021005 (2020); doi: 10.1116/1.5143203

Submitted: 20 December 2019 · Accepted: 9 March 2020 ·

Published Online: 25 March 2020



Pietro Benettoni,<sup>1</sup> Jia-Yu Ye,<sup>1,2</sup> Timothy R. Holbrook,<sup>3</sup> Federica Calabrese,<sup>1</sup> Stephan Wagner,<sup>3</sup>   
Mashaalah Zarejousheghani,<sup>4,5</sup> Jan Griebel,<sup>6</sup> Maria K. Ullrich,<sup>3</sup> Niculina Musat,<sup>1</sup>   
Matthias Schmidt,<sup>1</sup>   
Roman Flyunt,<sup>6</sup>   
Thorsten Reemtsma,<sup>3,7</sup>   
Hans-Hermann Richnow,<sup>1</sup>   
and Hryhoriy Stryhanyuk<sup>1,a)</sup> 

## AFFILIATIONS

<sup>1</sup>Department of Isotope Biogeochemistry, Helmholtz Centre for Environmental Research—UFZ, Permoserstraße 15, 04318 Leipzig, Germany

<sup>2</sup>Institute of Macromolecular Chemistry, Albert-Ludwigs-University of Freiburg, Stefan-Meier-Str. 31, 79104 Freiburg, Germany

<sup>3</sup>Department of Analytical Chemistry, Helmholtz Centre for Environmental Research—UFZ, Permoserstraße 15, 04318 Leipzig, Germany

<sup>4</sup>Institute of Electronic and Sensor Materials, Faculty of Materials Science and Materials Technology, TU Bergakademie Freiberg, Gustav-Zeuner-Straße 3, 09596 Freiberg, Germany

<sup>5</sup>Department of Monitoring and Exploration Technologies, Helmholtz Centre for Environmental Research—UFZ, Permoserstraße 15, 04318 Leipzig, Germany

<sup>6</sup>Leibniz Institute of Surface Engineering (IOM), Permoserstraße 15, 04318 Leipzig, Germany

<sup>7</sup>Institute of Analytical Chemistry, University of Leipzig, Linnéstrasse 3, 04103 Leipzig, Germany

**Note:** This paper is part of the 2020 Special Topic Collection on Secondary Ion Mass Spectrometry, SIMS.

**a) Author to whom correspondence should be addressed:** [gregory.stryhanyuk@ufz.de](mailto:gregory.stryhanyuk@ufz.de)

## ABSTRACT

Nowadays, high-resolution imaging techniques are extensively applied in a complementary way to gain insights into complex phenomena. For a truly complementary analytical approach, a common sample carrier is required that is suitable for the different preparation methods necessary for each analytical technique. This sample carrier should be capable of accommodating diverse analytes and maintaining their pristine composition and arrangement during deposition and preparation. In this work, a new type of sample carrier consisting of a silicon wafer with a hydrophilic polymer coating was developed. The robustness of the polymer coating toward solvents was strengthened by cross-linking and stoving. Furthermore, a new method of UV-ozone cleaning was developed that enhances the adhesion of the polymer coating to the wafer and ensures reproducible surface-properties of the resulting sample carrier. The hydrophilicity of the sample carrier was recovered applying the new method of UV-ozone cleaning, while avoiding UV-induced damages to the polymer. Noncontact 3D optical profilometry and contact angle measurements were used to monitor the hydrophilicity of the coating. The hydrophilicity of the polymer coating ensures its spongelike behavior so that upon the deposition of an analyte suspension, the solvent and solutes are separated from the analyte by absorption into the polymer. This feature is essential to limit the coffee-ring effect and preserve the native identity of an analyte upon deposition. The suitability of the sample carrier for various sample types was tested using nanoparticles from suspension, bacterial cells, and tissue sections. To assess the homogeneity of the analyte distribution and preservation of sample integrity, optical and scanning electron microscopy, helium ion microscopy, laser ablation inductively coupled plasma mass spectrometry, and time-of-flight secondary ion mass spectrometry were used. This demonstrates the broad applicability of the newly developed sample carrier and its value for complementary imaging.

© 2020 Author(s). All article content, except where otherwise noted, is licensed under a Creative Commons Attribution (CC BY) license (<http://creativecommons.org/licenses/by/4.0/>). <https://doi.org/10.1116/1.5143203>

## I. INTRODUCTION

High-resolution imaging techniques are often applied sequentially to complement each other and facilitate a comprehensive understanding of physical, chemical, and biological phenomena. A commonly employed complementary approach combines electron microscopy (EM) with secondary ion mass spectrometry (SIMS), thus providing high-resolution EM imaging together with elemental, molecular- and isotope-resolved SIMS analysis.<sup>1–3</sup> To further increase the resolution and obtain more surface-detailed images, helium ion microscopy (HIM) may also be applied in combination with EM and SIMS.<sup>4</sup> Electron- and ion-probe experiments require an ultrahigh vacuum (UHV) sample environment and demand distinct sample properties (e.g., regarding thickness, roughness, conductivity, etc.), and, therefore, samples have to be prepared differently according to instrument requirements.<sup>5</sup> For the implementation of complementary imaging analysis, a common sample carrier has to meet the requirements of the different imaging techniques involved.

At the same time, many analytical techniques face the challenge of an inhomogeneous analyte distribution upon deposition on a carrier surface. In particular when the analyte is nanosized, ion-, laser-, and electron-beam microscopes struggle to find a representative field of view (FoV). This leads to an extensive and time-consuming search for an optimal FoV for analysis. The two main effects that cause an inhomogeneous distribution of analytes deposited from suspensions on a solid surface are (i) the so-called “coffee-ring effect,” which takes place when suspended particles in a solution are carried to the outer edge of a spot after deposition due to the capillary flow in a drying sample<sup>6–8</sup> and (ii) the presence of contaminants that adhere to the carrier surface and render it hydrophobic.<sup>3–5</sup> Organic molecules adhered to the surface change the chemical and physical properties of the surface. This contamination can alter the native composition of the sample and change the surface polarity affecting, for example, the adhesion. Adhesion of hydrophobic compounds is a well-known phenomenon that occurs to a surface exposed to ambient air and even in UHV environments.<sup>9,10</sup> In particular for surface-sensitive analytical techniques such as Auger electron spectroscopy (AES) and X-ray photoelectron spectroscopy (XPS), the deposition of hydrocarbons presents a major challenge. Lately, manufacturers of semiconductor, electronic, and optical components have also focused their attention on this issue due to its disruptive effect at the interfaces in multilayered structures.

To recover the native surface properties (hydrophilicity, adhesion, etc.), the hydrocarbon contaminants have to be removed. UV-ozone cleaning was proved to be an effective method to remove surface contaminants<sup>11–13</sup> and was successfully employed for a variety of materials such as Si (SiO<sub>x</sub>), GaAs, SiC, Au, Ge, Ti, and Fe.<sup>14,15</sup> UV-ozone treatment is not only applied to inorganic but also to organic surfaces. Such treatment improves the wettability of these surfaces, allows good adhesion of surface finishing such as paints or inks, and also restores the hydrophilicity of a polymer after hydrophobic recovery.<sup>16,17</sup> However, the UV-ozone cleaning of organic materials without UV-induced damages of molecular structures is challenging due to their sensitive and fragile nature.<sup>11,18–20</sup> To limit this problem, in recent years, both organic and inorganic UV

absorbers have been mixed with organic coatings to reduce their photodegradation.<sup>20–22</sup> Nevertheless, the addition of these UV absorbers inevitably leads to the modification of the original properties of the polymers.

In order to address these challenges, we propose a new approach for the preparation of samples for high-vacuum imaging techniques. A new sample carrier comprising of a silicon (Si) wafer coated with a cross-linked polymer was developed. The hydrophilicity of the polymer coating is a key feature that ensures the transfer of solutes from the analyte suspension into the polymer layer, thus preventing analyte aggregation caused by the crystallization of salt contaminants and limiting the “coffee ring” effect. Furthermore, to meet the challenge of hydrophobic compounds adhering to the sample carrier surface, we developed the new UV-ozone cleaner “PULC-120.” The UV-ozone cleaner achieves maximum cleaning efficiency of a surface by exposure to reactive oxygen species (ROS), while at the same time shielding the organic polymer from direct UV irradiation.<sup>23</sup> The suggested sample carrier can accommodate a wide variety of analytes (e.g., NPs from suspensions, cells, biofilms, tissue sections, thin sections, etc.), undergo different preparation steps, and, therefore, allows the straightforward implementation of complementary imaging studies.

## II. EXPERIMENT

### A. Preparation of cross-linked polymer solution

To improve the robustness of the sample carrier toward solvents, the polymer was cross-linked following the protocol provided by the manufacturer.<sup>24</sup> The cross-linked polymer was prepared by the mixture of one solution containing the polymer with the cross-linker and the one containing the catalyst. The polymer solution was prepared as follows: 14 g Mowital B 30 T (Kuraray Europe GmbH, Hattersheim am Main, Germany) was dispersed in 27.2 ml ethanol denatured with 1% methyl ethyl ketone (Sigma-Aldrich, Merck KGaA, Darmstadt, Germany), 34.8 ml *n*-butanol (1-Butanol, Sigma-Aldrich, B7906), and 24.7 ml xylene (isomeric mixture, Merck, Darmstadt, Germany). The bottle with the solution was horizontally placed on a shaking platform (Multifunctional Orbital Shaker PSU-20i, Biosan, Riga, Latvia) overnight with an orbital speed of 250 rpm (reciprocal and vibro parameters kept off) until the Mowital powder was completely dissolved. Afterward, 11.7 ml Cymel 303 LF Resin (Methoxymethyl melamine, Allnex, Frankfurt, Germany) was added and the bottle was shaken for 1 h. The bottle was then stored in the dark to release the trapped bubbles overnight. The catalyst solution was prepared by mixing 0.23 ml of phosphoric acid (HPLC purity, Thermo Fisher Scientific, Massachusetts, USA) with 0.49 ml of *n*-butanol. At last, the acid solution was blended with the polymer solution and put on a shaker (PTR-35 360° Vertical Multifunction Rotator, Grant Instrument, Cambridge, UK) with reciprocal: 45°/30 s (vibro and orbital parameters kept off) for 4 h.

### B. Polymer deposition

Conductive Si wafers of 10 × 10 mm<sup>2</sup> size (boron-doped, Plano GmbH, Wetzlar, Germany) were chemically cleaned with ethanol in ultrasonic bath (SONOREX DIGITEC, BANDELIN

electronics GmbH, Berlin, Germany) for 15 min. The chemically cleaned Si wafer was either used as a control substrate for analyte deposition or underwent further UV-ozone treatment prior to coating with polymer. The polymer layer was deposited using a spin coater (SCI Series, LOT-QuantumDesign GmbH, Darmstadt, Germany). After starting the rotation, 250  $\mu\text{l}$  of cross-linked polymer were injected and spun at 50 ~ 60 revolutions per second (rps) for 2 min. An *ad hoc* lid of the spin coater was designed with two inlets that were connected to the argon purge at 8 l/min flow to shield the spinning solution from contaminants and dust. After spin coating, the carrier underwent stoving for 3 h in a  $10^{-2}$  mbar vacuum at 80 °C to remove remaining impurities and solvents from the reaction. Optimization of the stoving temperature was performed within the 80–160 °C range. Afterward, to rehydrophilize the polymer surface, the newly developed PULC-120 UV-ozone cleaner (extended description in Fig. S-1)<sup>48</sup> was applied with the reaction cell containing a 1 mm thick MgF<sub>2</sub> VUV-window (Korth Kristalle GmbH, Kiel, Germany). Finally, the sample carrier was ready for the analyte deposition.

### C. Contact angle measurements

The hydrophilicity of the surface was evaluated by contact angle (CA) measurements (contact angle measuring system G2, KRÜSS, Hamburg, Germany). The carriers were placed on the sample stage and the height of the stage, the position of the needle and the distance between the sample and camera were adjusted accordingly. A sessile drop of 2  $\mu\text{l}$  de-ionized water was applied on the surface, and the baseline was manually adjusted to fit the surface of the carriers. The contact angle of the water drop was determined by the average of ten measurements from both the right and the left side, respectively.

### D. Noncontact 3D optical profilometry

The thickness of the polymer layer was determined by a non-contact 3D optical profiler (S-Neox, Sensofar, Barcelona, Spain). Three scratches by razor blade were manually made and, under 10 $\times$  lens (NA = 0.65; WD = 17 mm), an optimal field of view was selected to measure the step between the Si wafer and the polymer. Afterward, a 100 $\times$  lens (NA = 0.95; WD = 0.3 mm) was used to image the selected field of view with a z-scan of 10  $\mu\text{m}$  with 0.1  $\mu\text{m}$  step. Finally, the thickness was determined by the average of the three different spots from three scratches. The noncontact 3D optical profiler was also used to observe the variation of the thickness of the cross-linked polymer deposited onto the Si wafer, after exposure to ethanol, acetone, and de-ionized water for 2 and 24 h.

### E. Absorption spectroscopy

The optimization of the O<sub>3</sub> production was achieved by using a spectrophotometer (67 Series, Jenway, Staffordshire, UK) to measure the continuous flow-through gas product via a gas cell (Cylindrical cells, Hellma Optik GmbH, Jena, Germany). The spectrophotometer was connected in line to a BMT device (BMT 964 BT, Messtechnik GmbH, Berlin, Germany), which quantified the O<sub>3</sub> concentration and finally to an O<sub>3</sub> quencher (BMT Heated CAT, Messtechnik GmbH, Berlin, Germany). The O<sub>2</sub> and N<sub>2</sub>

amount in the process chamber and the pulse energy of the Xe-lamp within the UV-ozone cleaner were varied systematically, and the absorbance and concentration of O<sub>3</sub> were recorded.

### F. Fourier-transform infrared spectroscopy (FTIR)

Infrared spectra measurements were carried out by a Cary 600 Series FTIR (Agilent Technologies Deutschland GmbH, Waldbronn, Germany) with the wavenumber between 800 and 4000  $\text{cm}^{-1}$ . Background measurements were done with germanium crystal for eight scans, and each spectrum was the result of four scans under an attenuated total reflectance (ATR) mode.

### G. Sample preparation for suspension

A stock solution of 56.8 mg/l Au NPs capped with citric acid (BBI solutions, Crumlin, UK) was sonicated (Bandelin Sonorex Digitec DT 1028 CH, Berlin, Germany) for 15 min and vortexed (Digital Vortex-Genie 2, Scientific Industries, Inc., New York, USA) at 2850 rpm for 5 min to resuspend the NPs. Afterward, 5  $\mu\text{l}$  of suspension were deposited onto polymer-coated carrier and noncoated Si wafer.

*Pseudomonas putida* mt-2 KT2440 (DSM6125) was routinely cultivated in 250 ml flasks containing 50 ml of nutrient broth (5 g/l peptone and 3 g/l meat extract) and 10% of inoculum at 30 °C under shaking. For cell suspension preparation, 2 ml of the culture were collected into two 2 ml sterile tubes (1 ml each), centrifuged three times at 12 500  $\times$  g for 10 min at room temperature (RT), washed with sterile cacodylate buffer (CaB), and finally, suspended in 2 ml of 3% glutaraldehyde in CaB. Cells were fixed for 2 h at RT, then washed twice to remove excess of fixative with CaB via centrifugation at 12 500  $\times$  g for 10 min at RT and resuspension in 2 ml of fresh CaB. A volume of 5  $\mu\text{l}$  was found to yield the best compromise between the volume cell number and cell distribution in a monolayer. Therefore, 5  $\mu\text{l}$  of the diluted cell suspension was deposited on the freshly UV-ozone treated sample carrier and left under the fume hood for 5 min in order to favor bacteria attachment to the polymer before dehydration. The sample was then dehydrated via increasing ethanol concentration in water-solution series (30, 50, 70, 80, 90, 96, and 100%), moving gently to avoid cell detachment. Afterward, the sample was dried upon 20 cycles of Critical Point Drying (EM CPD 300a, Leica, Vienna, Austria) and stored in a vacuum cabinet prior to analysis. As a control, the same amount of cells was filtered with a stainless steel syringe filter holder (Sartorius) onto a GTTP filter (0.22  $\mu\text{m}$  pore size, 25 mm diameter, GTTP02500, Merck, Darmstadt, Germany) coated with 20 nm Au/Pd (80/20) layer employing a sputter coater (EM SCD500, Leica, Vienna, Austria). The steps of dehydration with graded ethanol series were performed entirely inside of the filter holder, and the filter was removed at the end to undergo the CPD treatment.

### H. Sample preparation for tissue sections

Maize roots were chemically fixed in 2% paraformaldehyde (PFA) in CaB. The root sample was further dehydrated by exposure to increasing ethanol concentrations (30%, 50%, 70%, 90%, and 100%) for 10 min each and embedded at low temperature in Lowicryl K4 M (Agar Scientific Ltd., Stansted, UK). After embedding, the resin

blocks were stored under vacuum. Trimming of the resin block was performed with razor blades and an EM Trimming Leica machine. Semithin sections (200–400 nm thick) were then obtained using an ultramicrotome (EM UC7, Leica, Vienna, Austria) with a Diatome Ultra 45° knife (DiATOME, Hatfield, USA) and rapidly collected from the water. Initially, the sections were placed on a glass slide and observed with an optical microscope to check the quality of the section and the position of the region of interest on the section. Further on, consecutive sections were placed on the hydrophilic polymer-coated carrier and onto noncoated Si wafer for comparison.

A sample of frozen skin tissue from a New Zealand white rabbit was cryosectioned using a Microm HM 560 cryostat (Thermo Fisher Scientific GmbH, Dreieich, Germany). Thin sections with a thickness of 16 μm were cut and transferred immediately onto a pre-cooled hydrophilic polymer-coated carrier. For comparison, additional thin sections were placed onto noncoated carriers. All thin sections were thawed and dried in an evacuated desiccator and stored under vacuum ( $10^{-3}$  mbar) until analysis.

### I. Optical light microscopy

Overview images of the Au NPs and *Pseudomonas putida* were obtained with an optical microscope with circular differential interference contrast (C-DIC mode, Axio Scope.A1 microscope, Carl Zeiss Microscopy GmbH, Jena, Germany). After optical light microscopy investigation, the samples were further analyzed by scanning electron microscopy (SEM) and HIM.

Overview of tissue sections were obtained by Axio Imager.Z2 (Carl Zeiss Microscopy GmbH, Oberkochen, Germany) with an EpiPlan Neofluar 10× objective and with a binocular microscope (M205FA, Leica Microsystems GmbH, Wetzlar, Germany) with a PLANAPO 2× objective.

### J. Scanning electron microscopy and helium ion microscopy

A Merlin VP Compact SEM instrument (Carl Zeiss Microscopy GmbH, Oberkochen, Germany) was employed to visualize the Au NPs distribution on the sample carrier. Images were acquired with an electron acceleration voltage of 10 kV involving charge compensation that maintained the pressure in the analysis chamber at  $6 \times 10^{-3}$  mbar. Additionally, SEM was used with 45° sample-tilt and electron acceleration voltage of 5 kV to image the rabbit skin sections deposited onto the bare silicon wafer and polymer-coated carrier. *Pseudomonas putida* cells were imaged in secondary electron intensity with a HIM ORION NanoFab instrument (Carl Zeiss Microscopy, Peabody MA, USA) and operated at 25–30 keV energy of He<sup>+</sup> ions with a 0.02 pA probing beam. Charge compensation was also implemented with a flooding electron gun.

### K. Laser ablation inductive coupled plasma mass spectrometry (LA-ICP-MS)

The elemental distribution in a deposited air-dried spot of 5 μl Au NP suspension on the surface of the sample carrier was analyzed by elemental imaging with LA-ICP-MS. The LA-ICP-MS unit consisted of an Analyte G2 equipped with a Helix II sample chamber (Teledyne CETAC Technologies Inc., Bozeman, MT, USA)

and a Sector Field ICP-MS (Spectro, Ametek, Kleve, Germany). The ICP-MS allows simultaneous detection of multiple isotopes, which allows imaging of several elements at the very same ablation point. The instrumental conditions are summarized in Table S-1.<sup>48</sup> During ablation, the isotopes <sup>197</sup>Au, <sup>12</sup>C, <sup>28</sup>Si, and <sup>23</sup>Na were monitored at an integration time of 1 s. Additional experimental conditions are described in Table S-1.<sup>48</sup> From the transient intensity data, elemental distributions were reconstructed using HDIP v1.2.4d0 software.

### L. Time-of-flight secondary ion mass spectrometry (ToF-SIMS)

The spatial distribution of the Au nanoparticles as well as the solutes from suspension was further studied by a ToF-SIMS.5 instrument (IONTOF GmbH, Münster, Germany). Bi<sub>3</sub><sup>+</sup> cluster ions of 30 keV energy from liquid metal ion gun (LMIG NanoProbe) were employed as analysis gun. After each primary beam shot, the build-up charge above the sample was compensated with 15 eV electrons from flooding e-gun (FEG) and Ar gas injection system (Ar-GIS) upholding a partial Ar gas pressure of  $4 \times 10^{-6}$  mbar in the analysis chamber. The 250 eV Cs<sup>+</sup> projectile was employed as sputtering ion source to homogeneously remove organic and inorganic material as well as to enhance the yield of negative secondary ions. A delayed extraction mode was employed in the measurements providing a mass resolving power above 5000 and a lateral resolution of about 110 nm.

## III. RESULTS AND DISCUSSION

### A. Submolecular dry surface cleaning

Surface-cleaning employing UV-light and reactive oxygen species (referred as UV-ozone cleaning) is extensively used in industrial applications (e.g., coating, lithography, etc.) to eliminate residues of organic detergents as well as the adsorbed molecules.<sup>15–17,25–27</sup> The main advantages of UV-ozone cleaning are the short treatment time and the ambient pressure at which the process is carried out.<sup>12–14</sup> Furthermore, when compared with other commonly used surface treatments like cold-plasma cleaning, the surface after UV-ozone treatment shows better stability when exposed to air.<sup>17</sup> Nevertheless, the conventional UV-ozone cleaners available on the market face the limitation in their applicability to sensitive organic surfaces due to the following reasons:

- (i) long-lasting direct irradiation with UV-light;
- (ii) a continuous light source bringing a strong thermal load to the sample;
- (iii) fixed working distance not allowing to adjust the attenuation of the UV-light by the gas between the sample and the light source;
- (iv) open gas system (if any) not allowing to exploit the gas-flow geometry to guide the ROS toward the sample surface and not providing a possibility to control the composition of either the process-gas or the products of cleaning reaction;<sup>28</sup> and
- (v) the emission spectrum of the widely used mercury lamp in narrow spectral lines (183 and 253 nm) not being optimal for oxygen splitting.<sup>29,30</sup>

In the newly developed pulsed ultraviolet-light cleaner (PULC-120, detailed description in Fig. S-1),<sup>48</sup> a pulsed xenon discharge lamp with a MgF<sub>2</sub>-window is employed.<sup>23</sup> The lamp emits photons with a wavelength from 120 nm to the visible light range. The absorption coefficient of oxygen in the 140–160 nm spectral range emitted by the xenon lamp is up to 100 times higher than at 183 nm for a mercury lamp, leading to a higher O<sub>3</sub> production.<sup>30</sup>

The closed gas system of the PULC-120 instrument allows us to control the composition of the process gas mixture (O<sub>2</sub>/N<sub>2</sub>), the gas flow, the pressure, and temperature in the process chamber and to analyze the gas composition at the instrument exhaust. The composition and the flow rate of the process gas were optimized for maximum yield of ozone monitored with a spectrophotometer detecting the absorption of ozone at 254 nm (Fig. S-2A).<sup>48</sup> The ozone concentration was determined at different discharge energies of the xenon lamp (from 0.08 to 0.5 J) and was related to the corresponding absorption (Figs. S-2B and S-3).<sup>48</sup> In this way, a reproducible linear dependence between the UV pulse energy and ozone yield was shown.

With the optimized conditions, the surface of inorganic samples with high radiation hardness (e.g., Si wafers) was cleaned in 2 min upon direct UV irradiation at 1.5 mm working distance and 0.5 J pulse energy. After the 2 min treatment, the contact angle of water on the Si-wafer surface was shown to be 0° (Fig. S-4),<sup>48</sup> demonstrating the successful cleaning. The duration of the efficient cleaning is in agreement with the 90 s required to achieve near-atomically clean surfaces reported by Vig.<sup>31</sup> The achieved short treatment time requires a fast stabilization of process temperature that is implemented in the PULC-120 cleaner via pretempering the process gas mixture.

For the cleaning of organic samples, a reaction cell (schematically shown in Fig. 1) was introduced into the process chamber to

(i) minimize the photodegradation of the sample induced by UV radiation and (ii) maintain an efficient oxidation of surface contaminants with ROS. In the reaction cell, the process gas mixture is introduced through inlets (blue arrows in Fig. 1) distributed radially under the xenon lamp. The volume of the reaction cell is divided into two compartments separated by an intermediate optical filter. In the upper compartment, molecular oxygen (O<sub>2</sub>) is split into atomic oxygen (O) with hard VUV radiation from the xenon flash-lamp [Fig. 1(a)]. Atomic oxygen reacts quickly with other oxygen molecules and with nitrogen, introduced as a collision partner, to form ozone molecules (O<sub>3</sub>). In this compartment, the absorption of molecular oxygen up to 200 nm attenuates the VUV radiation from the xenon lamp. The attenuation can be enhanced by increasing the O<sub>2</sub> content in the process gas or by shifting the absorption edge of the intermediate filter toward 200 nm (i.e., changing the filter material from MgF<sub>2</sub> to quartz, sapphire, YAG). Ozone has a lifetime of about 20 min (at normal pressure and room temperature) that allows it to leave the upper compartment through the holes around the intermediate window [Fig. 1(b)] and to flow into the lower compartment [Fig. 1(c)], hosting the sample to be treated. The UV radiation transmitted through the upper compartment and the intermediate filter causes the photodissociation of ozone (Hartley absorption band with about 253 nm maximum) just above the surface to be cleaned. The absorption of UV-light by ozone above the sample attenuates the VUV radiation within 200–320 nm spectral range. Thus, due to the optimized geometry of the reaction cell, the light from the xenon lamp loses the hard VUV-UV component (120–320 nm) before reaching the sample surface limiting the photodegradation when treating sensitive organic materials.<sup>11,18</sup> The ROS produced upon O<sub>3</sub> photodissociation oxidize the topmost molecular layer by attacking C–C and C–H bonds [Fig. 1(c)]. Upon this oxidation, H<sub>2</sub>O and CO<sub>x</sub> are formed. H<sub>2</sub>O can further form hydroxyl radicals (•OH) in the presence of O<sub>3</sub> and UV-light that are highly oxidizing ROS.<sup>32,33</sup> The surface oxidation products leave the process chamber together with the N<sub>2</sub> and O<sub>x</sub> residuals through outlet holes in the sample tabletop.

## B. Polymer coating

Silicon wafers were selected for the carrier development due to their availability, low-cost, surface stability, and tunable conductivity. The wafers were coated with a polymer to modify their surface polarity. Polymers of the Mowital family were selected due to their purity, mechanical hardness, and variability in the degrees of viscosity and surface polarity. Within this family, polymers of T-grade have the highest hydrophilicity, with Mowital B 60 T being the most hydrophilic one. However, its solution was too viscous at the concentration required for volume-cross-linking to be spin-coated. Therefore, Mowital B 30 T polymer was selected as the best compromise between hydrophilicity and viscosity. As described previously, Mowital B 30 T can behave like a sponge and allow the transfer of water and solutes from the suspension drop into the polymer layer while keeping the analyte well attached.<sup>34</sup>

However, Mowital B 30 T alone turned out not to be resistant to either acetone or ethanol (Table S-2).<sup>48</sup> Cross-linking, which was previously shown to enhance the adhesion and resistivity of the polymer layer,<sup>35,36</sup> yielded only partial improvement in this case

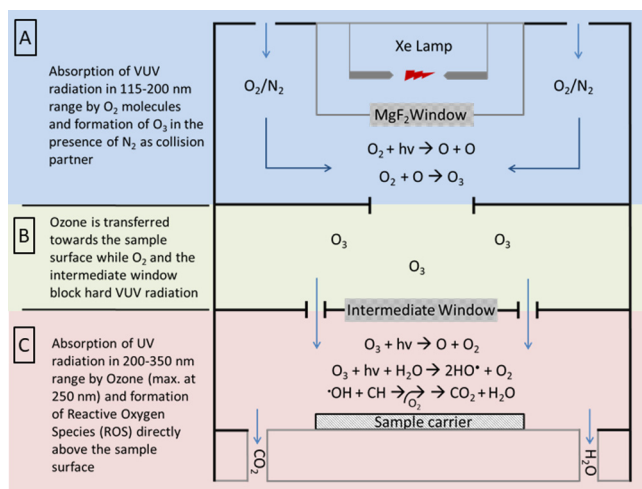


**FIG. 1.** Schematic representation of the reaction cell to be inserted into the process chamber of the PULC-120 UV-ozone cleaner. (a) Upper compartment, where O<sub>2</sub> is split in O atoms that react with N<sub>2</sub> and other O<sub>2</sub> molecules to form O<sub>3</sub>. (b) Ozone leaves the upper compartment through the holes around the intermediate window and flows into the lower compartment (c), where the ROS are formed above the surface of the sample to be cleaned.

(Table S-2).<sup>48</sup> Stoving could improve it further, but upon stoving at 200 °C as suggested by the manufacturer,<sup>24</sup> the polymer became hydrophobic (CA about 74°, data not shown), likely due to the loss of OH-groups. Therefore, stoving was tested at temperatures of 80, 100, 120, 140, 160 °C in vacuum ( $5 \times 10^{-2}$  mbar) to determine the optimal temperature at which both resistivity and hydrophilicity requirements are fulfilled. All the sample carriers stoved at different temperatures were shown to be resistant to the solvents. After stoving, the sample carrier was treated for 2 min with the PULC-120 UV-ozone cleaner equipped with the reaction cell. As visible from the contact angle measurements, the hydrophilicity was the highest at the lowest stoving temperature of 80 °C [Fig. 2(a)]. The extremely low value of contact angle (CA: 14°) also confirms a successful removal of contaminants from the carrier surface by the subsequent UV-ozone cleaning. Hydrophilicity then decreased with the increase of the stoving temperature [Fig. 2(a)]. This development is explainable by Fourier-transformed infra-red spectrometry (FTIR) data shown in Fig. 2(b). Temperature-dependent changes are visible for the broad peak from 3200 to 3400  $\text{cm}^{-1}$  attributed to hydroxyl groups and the peak around 2400  $\text{cm}^{-1}$  attributed to the  $\text{CO}_2$  present in ambient air. Thus, the inset of Fig. 2(b) shows that the number of hydroxyl groups decreases with increasing stoving temperatures.

Aging of polymer-coated carriers was studied over 120 h in parallel to noncoated Si wafers. Contact angle measurements showed that the hydrophobicity increased over time due to the adsorbed contaminants for both the coated and noncoated Si wafer (Fig. 3). This phenomenon is well known from the literature and is described as “hydrophobic recovery.”<sup>37–39</sup> The increase of CA is more pronounced for the polymer-coated carrier possibly due to the stickiness of its surface enhancing the trapping of gas molecules. After 120 h both sample carriers were treated with the PULC-120 again. As shown in Fig. 3, PULC-120 is capable of restoring the hydrophilicity

of both, the polymer-coated and the noncoated carrier: the contact angle is reduced from 55° to 25° and from 45.8° to 0°, respectively. The efficiency of UV-ozone treatment to improve the wettability of polymers was recently also reported for the application of PMMA polymer in chip fabrication.<sup>17</sup> Nevertheless, the severe damages that UV light can cause to PMMAs<sup>40–42</sup> were neither taken into consideration nor monitored. Here, the treatment of an aged polymer layer with direct UV irradiation for 2 min in the PULC-120 without the reaction cell did not improve the hydrophilicity. In fact, the contact angle remained at 56.1° after this treatment (blue triangle in Fig. 3 and Fig. S-5),<sup>48</sup> implying that reversing the hydrophobic recovery is not possible without the reaction cell. The direct exposure to UV radiation induced the photolysis of the polymer causing the disruption and translocation of polymer fragments on the topmost layer of the polymer that, therefore, remains hydrophobic (Fig. S-5).<sup>48</sup> The possibility to reverse the hydrophobic recovery shows that the PULC-120 provides an efficient and rapid method to clean not only inorganic material but also sensitive organic surfaces.

### C. Analyte deposition

The suitability of the polymer-coated carrier for different sample types and imaging applications was tested. Nanoparticles and microbial cell suspensions, as well as sliced tissue sections, were deposited onto the polymer-coated carrier.

#### 1. Analytes deposited from suspension

One of the challenges in analyzing particles from suspension by imaging techniques is to deposit them homogeneously on the sample carrier. The hydrophilicity of the polymer-coated sample carrier, recovered with the PULC-120 UV-ozone cleaner, allows the water together with its soluble components (i.e., salts) to penetrate into the polymer. Thus, the analyte is firmly attached to the

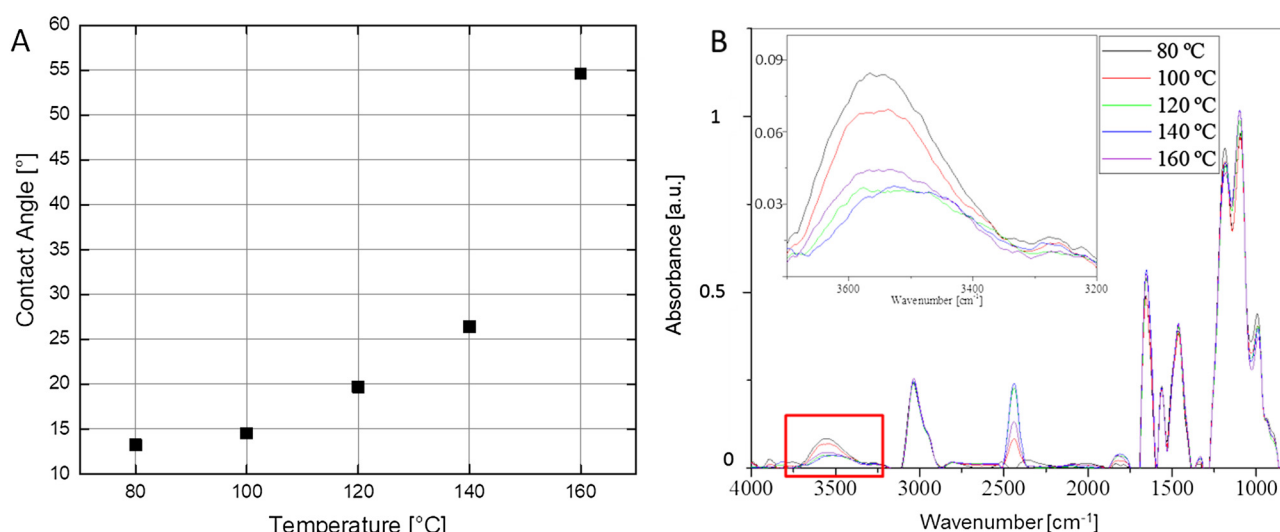


**FIG. 2.** Influence of stoving temperatures on the properties of the cross-linked polymer layer of the sample carrier hydrophilicity determined by water contact angle (a) and chemical composition detected by FTIR measurements (b). The inset in (b): magnification of wavenumbers from 3700 to 3200  $\text{cm}^{-1}$  attributed to OH groups.

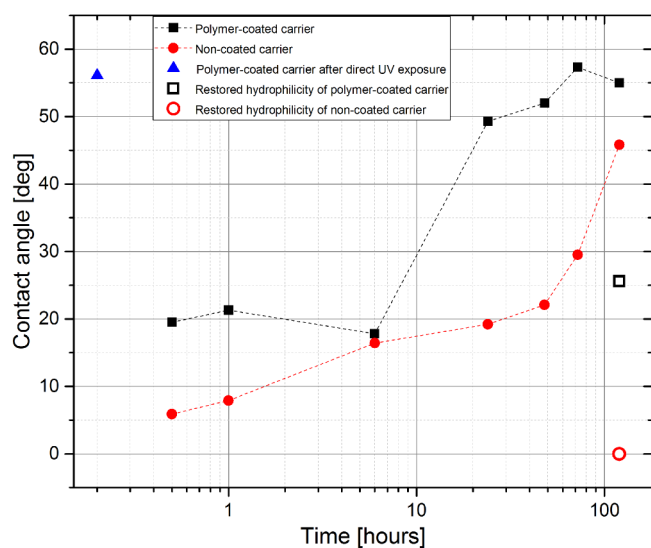


**FIG. 3.** Hydrophobic recovery monitored by water contact angle measurement over time after exposure to PULC-120 UV-ozone cleaner (time 0) up to 120 h of both the polymer-coated carrier (black solid squares) and the noncoated carrier (red solid circles). After 120 h exposure to ambient air, PULC-120 was used to restore the hydrophilicity of the polymer-coated carrier (open black square) and of the Si wafer (open red circle).

topmost layer of the polymer, while the solutes are confined and trapped within the polymer layer (Fig. 4).

Observation with optical microscopy (Fig. S-6)<sup>48</sup> revealed a homogeneous distribution of both NPs and cells over the whole area observed (i.e., ~150 μm). Further investigation to observe and quantify the homogeneity of the analyte was carried out with SEM, HIM, and LA-ICP-MS. SEM was used to image Au NPs with high-resolution and a homogenous NPs distribution over a large FoV (i.e., ~120 μm) is visible in Fig. 5. In these images, neither an aggregation nor a drying effect is visible as compared to the NPs

deposited on a noncoated Si wafer where the “coffee ring” effect is clearly visible (Figs. S-7A and S-7B).<sup>48</sup> Similarly, when imaging *Pseudomonas putida* with HIM [Fig. 5(b)], the cells are not forming the typical flocculation that is commonly occurring when cells are deposited onto a noncoated carrier after drying (Fig. S-7C).<sup>48</sup> A sticky polymer layer not only assures a good adhesion of the analyte during different preparations that involve mechanical stress (e.g., fluorescence *in situ* hybridization (FISH), water-ethanol/acetone exchange prior to CPD, etc.) but also helps us to prevent detachment, dislocation, or removal of nanosized analyte fractions when hit by an ion, electron, or laser beam.

LA-ICP-MS was used to determine the elemental distribution of Au NPs and salts residuals from the synthesis that are always present in the stock suspension of citrate coated Au NPs.<sup>34</sup> For this purpose, Au NPs stock suspension was deposited onto three different sample carriers: noncoated Si wafer [Figs. 6(a) and 6(b) and Figs. S-8A and S-8B],<sup>48</sup> hydrophobic polymer-coated carrier [Figs. 6(c) and 6(d) and Figs. S-8C and S-8D],<sup>48</sup> and hydrophilic polymer-coated carrier [Figs. 6(e) and 6(f) and Figs. S-8E and S-8F].<sup>48</sup> In Fig. 6, the intensities in both the chemical images and transients (Fig. S-8)<sup>48</sup> of Au<sup>+</sup> and Na<sup>+</sup> correspond to the analysis of the same sample droplet. In Figs. 6(a) and 6(b), the increased intensities at the edge of the droplet as well as the lower intensity in the middle of the droplet represent the coffee ring effect, which is clearly visible in Fig. 6(a) and in the transients (Figs. S-8A and S-8B).<sup>48</sup> These observations for the noncoated Si wafer further support the inhomogeneity visualized by previous microscopy techniques. Similarly, in Figs. 6(c) and 6(d), the hydrophobic sample carrier (i.e., nontreated with PULC-120 before NPs deposition) also shows an inhomogeneous distribution of salts [Fig. 6(c) and Fig. S-8C].<sup>48</sup> However, due to the sponge effect of the newly developed sample carrier even before treatment, the Au NPs appear to be distributed more homogeneously than on the noncoated Si wafer [Fig. 6(d) and Fig. S-8D].<sup>48</sup> In this image, the “coffee-ring” effect is still visible even if just at the outmost edge but no drying effect occurred after drying. The final UV-ozone treated sample carrier [Figs. 6(e) and 6(f)] shows a higher homogeneity of Au NPs over a bigger area (~5 mm) as well as a more uniformly

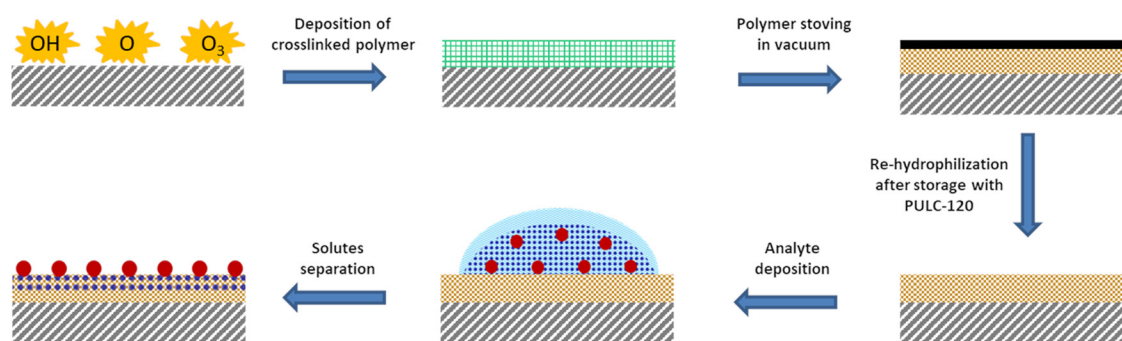


**FIG. 4.** Schematic representation of the workflow for the sample carrier preparation. From the treatment with PULC-120 UV-ozone cleaner to the adhesion of hydrocarbons during storage and the subsequent removal with a second UV-ozone treatment. Followed by the deposition of the analyte (red circles) and penetration of the solutes (dark blue circles) into the polymer.



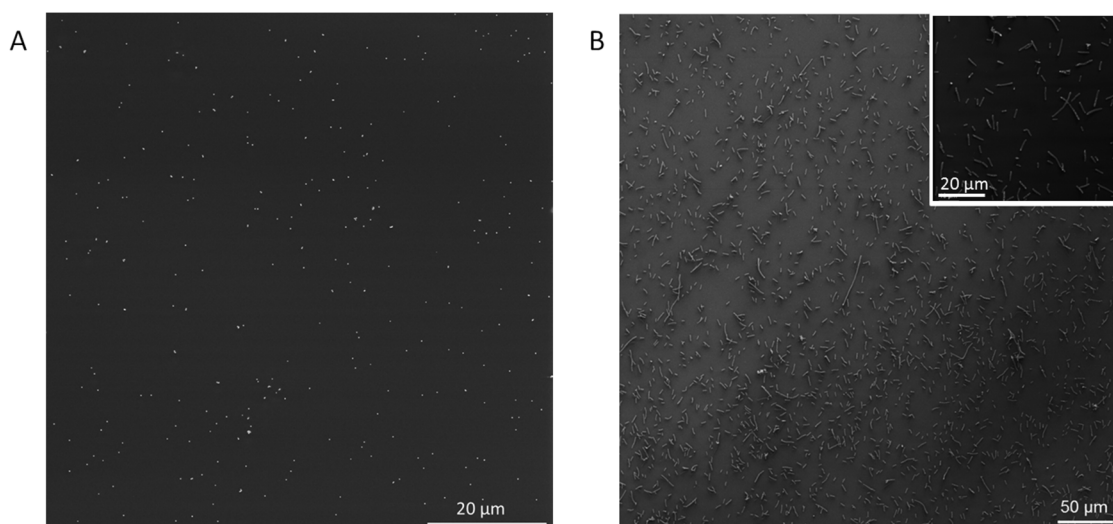


**FIG. 5.** High-resolution microscopy observations of Au 200 nm NPs with SEM (a) and *Pseudomonas putida* with HIM (b).

distributed Na<sup>+</sup> signal [Figs. 6(e) and Fig. S-8E].<sup>48</sup> Additionally, Fig. 6(e) shows the clear detection of Na<sup>+</sup> ion signal also outside of the area where the suspension was deposited. This effect is also visible in Fig. 6(c) even if it is less pronounced and not visible at all

when depositing the NPs onto the noncoated carrier. These observations are attributed to the high hydrophilicity of the new sample carrier and to the enhanced sponge effect that allows the separation of the soluble contaminants from the analyte and limits the

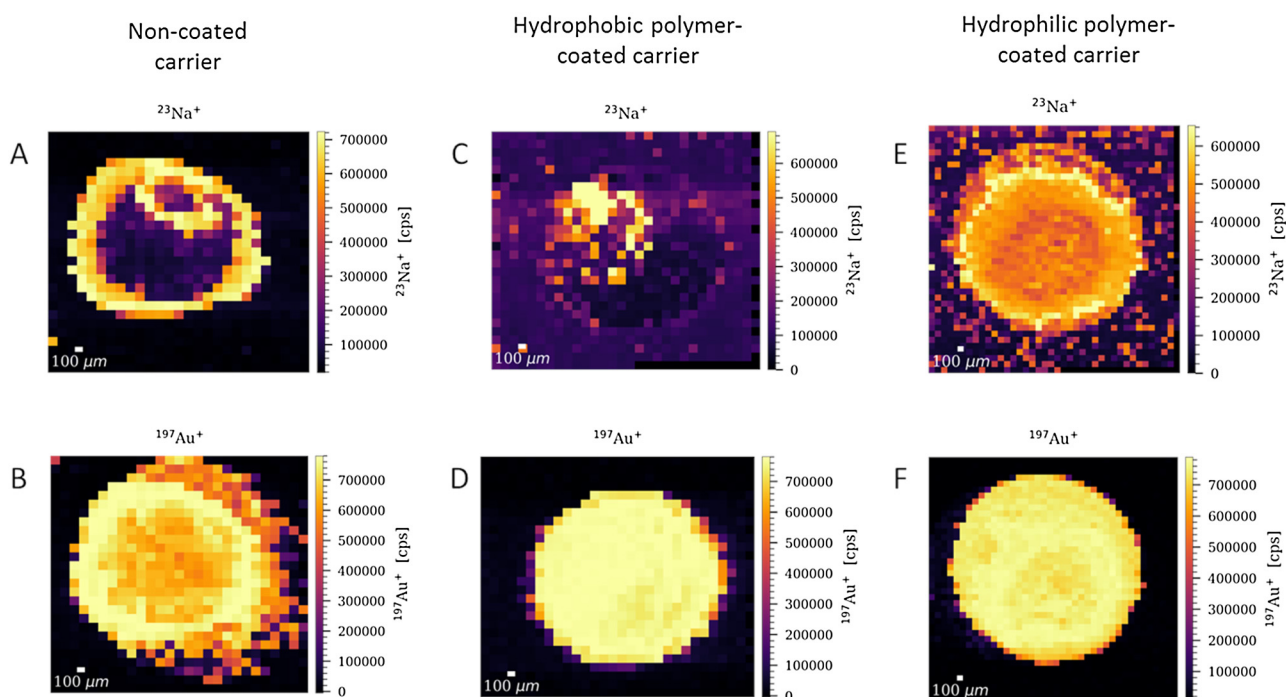


**FIG. 6.** Chemical images obtained via LA-ICP-MS analysis of Au NPs deposited on a naked Si wafer [(a) and (b)], an untreated sample carrier [(c) and (d)], and an UV-ozone treated sample carrier [(e) and (f)].

formation of the ring upon drying. The higher pixel density in the image of the hydrophilic polymer-coated sample [Figs. 6(e) and 6(f)] represents a larger spot diameter as compared to Figs. 6(a)–6(d). The increased diameter of the deposited analyte, also visible in the transients (Fig. S-8E and S-8F),<sup>48</sup> is attributed to the higher hydrophilicity and lower contact angle of the carrier.

The high-resolution ToF-SIMS experiment was performed to elucidate the separation of salts upon the deposition of 200 nm Au NPs from a suspension onto the polymer-coated carrier. For comparison, the analysis was also conducted with the same NPs deposited on noncoated Si wafers. The ToF-SIMS data in Fig. 7 show the distribution of analytes integrated in depth, and the corresponding depth profiles are presented in Fig. S-9.<sup>48</sup> The distribution of Au NPs (<sup>198</sup>Au<sup>-</sup> mass peak) and salts (Cl<sup>-</sup>, K<sup>-</sup>) as deposited on two types of carriers (with and without polymer coating) allowed comparing the homogeneity of particle and solutes distribution (Fig. 7). The distribution on the polymer-coated carrier [Figs 7(a)–7(d)] shows a clear reduction of the salts associated with the Au NPs. Due to this reduction, the salt crystallization does not occur on the carrier surface upon drying and the analyte particles stay separated and homogeneously distributed on top of the polymer layer [RGB overlay Fig. 7(d)]. The depth profiles shown in Fig. S-9 (Ref. 48) demonstrate the salts permeating the uppermost layer of the polymer-coating. In this figure, the polymer layer removed within initial 400 s of sputtering reveals an increased salt content, after which the salt-related signal decreased significantly toward a stable level at the silicon wafer. In Fig. 7(b), the Cl<sup>-</sup> ion yield appears to be colocalized with the NPs, suggesting only a partial separation of salts from the NPs. However, the ionization enhancement caused by Au NPs is a well-known effect in the literature.<sup>43–45</sup> Therefore, the metal might act as a probe of the surrounding environment

and ionize the salts in its close proximity. Nevertheless, the NPs are preferentially forming large aggregates when deposited on the non-coated wafer [Figs. 7(e)–7(h)], demonstrating the valuable advantage of the newly developed sample carrier. In fact, when comparing the distribution of the salt-related secondary ions (Cl<sup>-</sup>, K<sup>-</sup>) with the Au<sup>-</sup> signal, they are clearly colocalized [RGB overlay Fig. 7(h)]. Thus, the NPs are aggregated due to the crystallization of the salt contaminants upon drying.

The imaging analysis with electron-, ion-, and laser beam demonstrate the capabilities of the newly developed sample carrier to produce a homogeneous distribution of deposited suspensions. The homogeneous distribution together with the increased surface coverage of the deposited analyte allows (i) for single particles or single-cell analyses, (ii) subsequential deposition of the analyte without causing aggregation in suspension, (iii) the removal and reduction of soluble contaminants, (iv) a fast identification of a representative FoV, and (v) the possibility for absolute quantitative analyses for some analytical methods.

## 2. Tissue sections

Artifacts such as shrinkage and collapse of fragile structures are well-known issues that arise from air-dried biological samples.<sup>46</sup> Furthermore, for thin sections deposited onto a polycarbonate filter or Si wafer, there is a high risk to peel off during the preparation or staining process (e.g., DAPI, FISH) due to poor adhesion to the filter.<sup>47</sup> As a result, multiple sections need to be prepared to ensure that part of them will still be attached so that a sufficient number of samples is meeting the requirements for analysis.

Plant roots preserved in resin and frozen rabbit skin were cut in thin sections, deposited onto the coated and noncoated carriers

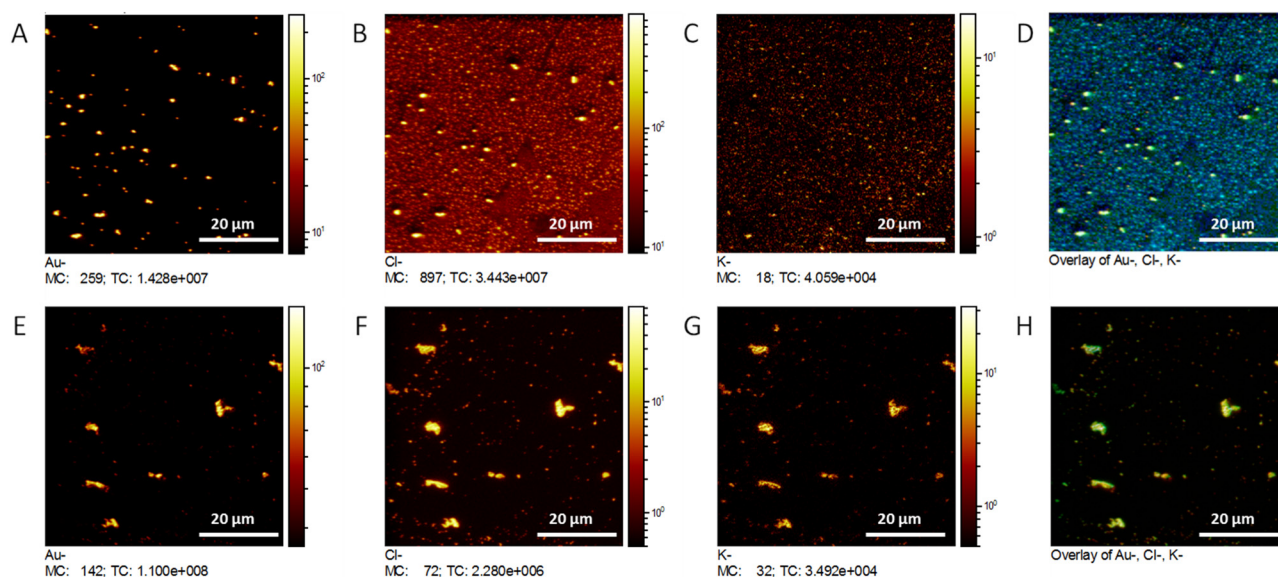


**FIG. 7.** ToF-SIMS chemical imaging of Au NP (Au<sup>-</sup>) and salt (Cl<sup>-</sup>, K<sup>-</sup>) solutes deposited on the polymer-coated sample carrier [(a)–(b)–(c)–(d)] and on the Si wafer [(e)–(f)–(g)–(h)]. (d) and (h) are RGB overlay of Au<sup>-</sup>, K<sup>-</sup>, Na<sup>-</sup> secondary ions in red, green, and blue, respectively.

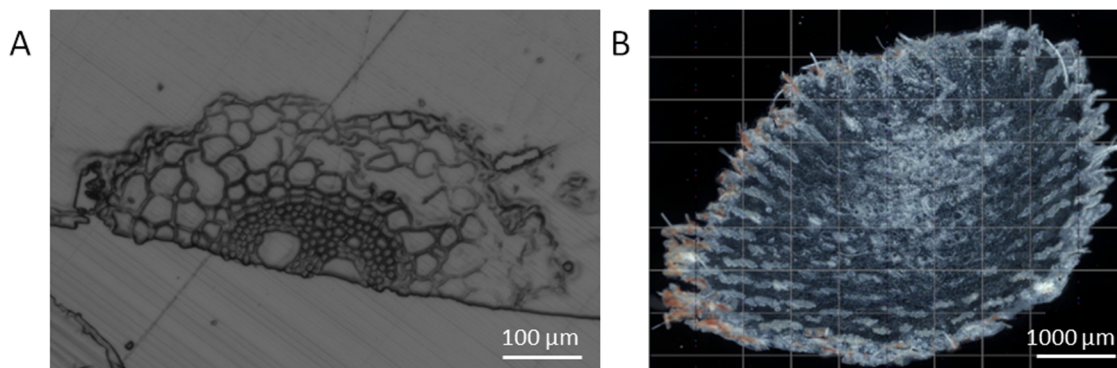


**FIG. 8.** Optical microscope observation of thin sections of plant root embedded in resin (a) and cryosectioned rabbit skin section (b) deposited on the polymer-coated sample carrier.

and stored under vacuum (i.e.,  $10^{-3}$  mbar). Afterward, the preservation of the original structural properties of the sections was examined with an optical light microscope (Fig. 8). Both the plant root and the skin section were well stretched and firmly attached to the polymer layer with only minor ripples or deformations from drying [Figs. 8(a) and 8(b)]. In fact, the hydrophilic character of the polymer allows the water to penetrate into the polymer layer and, therefore, an enhanced adhesion and stretching of the sections occur. When deposited on the noncoated carrier, already after storage at  $10^{-3}$  mbar, the root section appeared scrunched and many wrinkles were visible after drying (Fig. S-10A).<sup>48</sup> Similarly, the frozen skin tissue section deposited on the noncoated Si wafer showed major signs of detachment from the carrier, leading to significant topography across the entire thin section (Fig. S-10B).<sup>48</sup>

Further analysis of the rabbit skin sections with SEM confirmed the strong topography arising when the tissue section is deposited on the bare silicon wafer [Fig. 9(a)]. In this figure, the detachment of the section from the wafer is clearly visible, particularly in the center of the thin section. Furthermore, when looking at the boundaries between the sample and the substrate, salt crystals are present all around the section [Fig. 9(a)]. On the contrary, the section deposited onto the polymer-coated carrier appears flat, without detachment and salt residuals around [Fig. 9(b)]. In fact, when using the newly developed sample carrier, the sticky polymer prevents the shrinking and detachment of thin sections due to the permeation of the water and soluble contaminants into the uppermost layer of the polymer. Thus, the original structure of the tissue samples is preserved for subsequent analysis.

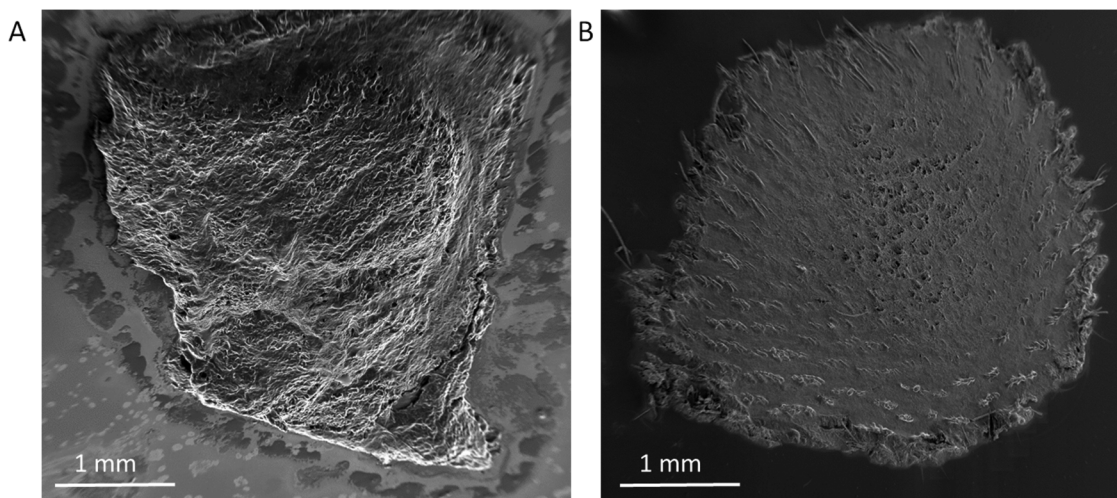


**FIG. 9.** High-resolution SEM images of frozen rabbit skin sections deposited onto (a) bare silicon wafer and (b) polymer-coated carrier.

#### IV. SUMMARY AND CONCLUSIONS

The wettability of the Si wafer was dramatically enhanced with the new optimized UV-ozone cleaner, and thus, an optimal deposition and adhesion of the polymer layer was achieved. After the polymer coating and a long storage of the sample carrier, the UV-ozone cleaner was applied again to modify the surface and restore the native hydrophilic character of the polymer. This further modification was shown to increase the surface wettability of the polymer by generating hydroxyl groups without photodamaging it. Additionally, in order to incorporate this sample carrier in well-known sample preparation workflows (e.g., CPD, staining, etc.) for ultrahigh vacuum microscopies, the polymer was cross-linked and underwent a stoving process to enhance its robustness and resistance to solvents. The high hydrophilicity of the sample carrier allowed a homogeneous analyte distribution after deposition and the removal of soluble contaminants from the topmost layer to the depth of the polymer. This separation is crucial for the analysis of single cells and single particles by high-resolution microscopy techniques. The wide applicability of the newly developed sample carrier was shown by the deposition of different analytes (i.e., NPs, cells, thin sections) and analysis with multiple complementary high-resolution imaging techniques. In particular, optical microscopy, SEM, and HIM were employed to demonstrate the homogeneous distribution of the analytes on the topmost layer of the sample carrier. Detailed information about multiple elements and the distribution of soluble contaminants in depths were obtained by LA-ICP-MS andToF-SIMS. In summary, the new sample carrier can (i) accommodate various analytes, (ii) preserve pristine arrangements and fragile structures, (iii) guarantee a homogeneous sample distribution, (iv) undergo different preparation steps, and (v) be compatible with multiple complementary ultrahigh vacuum techniques.

#### ACKNOWLEDGMENTS

The authors acknowledge funding from the ACENano project within the European Union Horizon 2020 program (H2020, Grant No. 720952). This research was carried out at the ProVIS Centre for Chemical Microscopy, which was established with the European Regional Development Funds (EFRE—Europe funds Saxony) at the Helmholtz Centre for Environmental Research and was supported by the Helmholtz Association. The authors would like to sincerely thank J. F. Kahn from Charité Hospital Berlin for providing frozen rabbit-tissue samples.

#### REFERENCES

- <sup>1</sup>K. L. Moore, E. Lombi, F. J. Zhao, and C. R. M. Grovenor, *Anal. Bioanal. Chem.* **402**, 3263 (2012).
- <sup>2</sup>J. H. M. Osorio *et al.*, *FEMS Microbiol. Ecol.* **95**, fiz029 (2019).
- <sup>3</sup>F. Vollnhals *et al.*, *Anal. Chem.* **89**, 10702 (2017).
- <sup>4</sup>T. Wirtz, P. Philipp, J. N. Audinot, D. Dowsett, and S. Eswara, *Nanotechnology* **26**, 434001 (2015).
- <sup>5</sup>J. Decelle *et al.*, *Trends Cell Biol.* **30**, 173 (2020).
- <sup>6</sup>R. D. Deegan, O. Bakajin, T. F. Dupont, G. Huber, S. R. Nagel, and T. A. Witten, *Nature* **389**, 827 (1997).
- <sup>7</sup>H. Hu and R. G. Larson, *J. Phys. Chem. B* **110**, 7090 (2006).
- <sup>8</sup>H. Hu and R. G. Larson, *J. Phys. Chem. B* **106**, 1334 (2002).

- <sup>9</sup>S. Berkebile and J. Gaier, “Adhesion in a vacuum environment and its implications for dust mitigation techniques on airless bodies,” in *42nd International Conference on Environmental Systems*, San Diego, California (American Institute of Aeronautics and Astronautics, San Diego, CA, 2012), pp. 1–10.
- <sup>10</sup>H. H. Brongersma, M. Draxler, M. de Ridder, and P. Bauer, *Surf. Sci. Rep.* **62**, 63 (2007).
- <sup>11</sup>D. A. Bolon and C. O. Kunz, *Polym. Eng. Sci.* **12**, 109 (1972).
- <sup>12</sup>J. Vig and J. LeBus, *IEEE Trans. Parts Hybrids Packag.* **12**, 365 (1976).
- <sup>13</sup>J. R. Vig, *J. Vac. Sci. Technol. A* **3**, 1027 (1985).
- <sup>14</sup>D. W. Moon, A. Kurokawa, S. Ichimura, H. W. Lee, and I. C. Jeon, *J. Vac. Sci. Technol. A* **17**, 150 (2002).
- <sup>15</sup>S. Bakhshi, N. Zin, H. Ali, M. Wilson, D. Chanda, K. O. Davis, and W. V. Schoenfeld, *Sol. Energy Mater. Sol. Cells* **185**, 505 (2018).
- <sup>16</sup>I. Mathieson and R. H. Bradley, *Int. J. Adhes. Adhes.* **16**, 29 (1996).
- <sup>17</sup>J. Liu *et al.*, *ACS Appl. Mater. Interfaces* **8**, 30576 (2016).
- <sup>18</sup>R. L. Feller, M. Curran, V. Colaluca, J. Bogaard, and C. Bailie, *Polym. Degrad. Stab.* **92**, 920 (2007).
- <sup>19</sup>D. Ghazi, G. El-Hiti, E. Yousif, D. Ahmed, and M. Alotaibi, *Molecules* **23**, 254 (2018).
- <sup>20</sup>S. Nikafshar, O. Zabihi, M. Ahmadi, A. Mirmohseni, M. Taseidifar, and M. Naebe, *Materials* **10**, 1 (2017).
- <sup>21</sup>R. R. Devi and T. K. Maji, *Ind. Eng. Chem. Res.* **51**, 3870 (2012).
- <sup>22</sup>F. Aloui, A. Ahajji, Y. Irmouli, B. George, B. Charrier, and A. Merlin, *Appl. Surf. Sci.* **253**, 3737 (2007).
- <sup>23</sup>Stryhanyuk, H. European patent EP3586986 (1 January 2020).
- <sup>24</sup>Kuraray Europe GmbH, *Guide Formulation* (2010).
- <sup>25</sup>M. Tabe, *Appl. Phys. Lett.* **45**, 1073 (1984).
- <sup>26</sup>T. Clark, J. D. Ruiz, H. Fan, C. J. Brinker, B. I. Swanson, and A. N. Parikh, *Chem. Mater.* **12**, 3879 (2000).
- <sup>27</sup>X. Jiang, F. L. Wong, M. K. Fung, and S. T. Lee, *Appl. Phys. Lett.* **83**, 1875 (2003).
- <sup>28</sup>Yoshiaki, I. European patent EP2177278A1 (21 April 2010).
- <sup>29</sup>J. M. Dohan and W. J. Masschelein, *Ozone Sci. Eng.* **9**, 315 (1987).
- <sup>30</sup>M. Salvermoser, D. E. Murnick, and U. Kogelschatz, *Ozone Sci. Eng.* **30**, 228 (2008).
- <sup>31</sup>Vig, J. R., Ultraviolet-Ozone Cleaning of Semiconductor Surfaces (Army Research Laboratory, Fort Monmouth, NJ, 1992).
- <sup>32</sup>G. R. Buettner, *Arch. Biochem. Biophys.* **300**, 535 (1993).
- <sup>33</sup>J. H. Seinfeld and S. N. Pandis, *Atmospheric Chemistry and Physics: From Air Pollution to Climate Change* (Wiley, New York, 2016).
- <sup>34</sup>P. Benettoni, H. Stryhanyuk, S. Wagner, F. Kollmer, J. H. Moreno Osorio, M. Schmidt, T. Reemtsma, and H.-H. Richnow, *J. Anal. At. Spectrom.* **34**, 1098 (2019).
- <sup>35</sup>G. T. Carroll, M. E. Sojka, X. Lei, N. J. Turro, and J. T. Koberstein, *Langmuir* **22**, 7748 (2006).
- <sup>36</sup>G. Wantz, L. Derue, O. Dautel, A. Rivaton, P. Hudhomme, and C. Dagron-Lartigau, *Polym. Int.* **63**, 1346 (2014).
- <sup>37</sup>S. Hemmilä, J. V. Cauich-Rodríguez, J. Kreutzer, and P. Kallio, *Appl. Surf. Sci.* **258**, 9864 (2012).
- <sup>38</sup>M. Mortazavi and M. Nosonovsky, *Appl. Surf. Sci.* **258**, 6876 (2012).
- <sup>39</sup>E. Bormashenko, G. Chaniel, and R. Grynyov, *Appl. Surf. Sci.* **273**, 549 (2013).
- <sup>40</sup>P. Henzi, K. Bade, D. G. Rabus, and J. Mohr, *J. Vac. Sci. Technol. B* **24**, 1755 (2006).
- <sup>41</sup>S. Eve and J. Mohr, *Proc. Eng.* **1**, 237 (2009).
- <sup>42</sup>M. Melo, S. Fernandes, N. Caetano, and M. T. Borges, *J. Appl. Phycol.* **30**, 887 (2018).
- <sup>43</sup>A. Delcorte, S. Yunus, N. Wehbe, N. Nieuwjaer, C. Poleunis, A. Felten, L. Houssiau, J. J. Pireaux, and P. Bertrand, *Anal. Chem.* **79**, 3673 (2007).
- <sup>44</sup>N. Wehbe, A. Heile, H. F. Arlinghaus, P. Bertrand, and A. Delcorte, *Anal. Chem.* **80**, 6235 (2008).

<sup>45</sup>O. Restrepo, A. Prabhakaran, K. Hamraoui, N. Wehbe, S. Yunus, P. Bertrand, and A. Delcorte, *Surf. Interface Anal.* **42**, 1030 (2010).

<sup>46</sup>A. M. Kashi, K. Tahermanesh, S. Chaichian, M. T. Joghataei, and M. Fateme, *Galen Med. J.* **3**, 63 (2014).

<sup>47</sup>C. Kuepper, A. Kallenbach-Thieltges, H. Juetten, A. Tannapfel, F. Großerueschkamp, and K. Gerwert, *Sci. Rep.* **8**, 7717 (2018).

<sup>48</sup>See [supplementary material](#) at for details on experimental design, instrument settings and additional results.